

# Tuning Terahertz Optomechanics of MoS<sub>2</sub> Bilayers with Homogeneous In-plane Strain

S. Patel,<sup>1</sup> Jose D. Mella,<sup>1</sup> S. Puri,<sup>1</sup> Salvador Barraza-Lopez,<sup>1,2</sup> and H. Nakamura<sup>1,\*</sup>

<sup>1</sup>Department of Physics, University of Arkansas, Fayetteville, Arkansas 72701, USA

<sup>2</sup>Institute for Solid State Physics, University of Tokyo, Kashiwa, 277-8581, Chiba, Japan

(Dated: February 13, 2026)

Homogeneous in-plane biaxial tensile strain strengthens the out-of-plane van der Waals interaction in MoS<sub>2</sub> bilayers (BLs) and can be used to fine-tune their terahertz (THz) oscillations. Using ultralow-frequency Raman spectroscopy on hexagonal (2H) and rhombohedral (2R) stacked BLs, we observe a hardening of the interlayer breathing modes originating from a strain-induced Poisson contraction of the vdW separation between the layers, and characterized by an effective out-of-plane Poisson's ratio of  $\nu_{\text{eff}} \approx 0.19\text{--}0.24$ . Strikingly, this geometric contraction drives the system into a highly repulsive regime of the intermolecular potential, corresponding to a Grüneisen parameter of  $\gamma \approx 10\text{--}14$ . This value surpasses even the 'giant' one reported for phosphorene, establishing these van der Waals BLs as highly tunable nonlinear mechanical platforms that can be addressed at the THz regime, couple strongly with light, and do not need external pressure knobs.

Weather monitoring, airport security, and high-bandwidth (6G) communications can all benefit from electromagnetic oscillators at the THz range [1, 2]. Anti-ferromagnets [3] and two-dimensional van der Waals materials [4, 5] are starting to be used to create and/or detect THz radiation. In turn, THz phonon vibrations could be useful for microwave acoustic filters, acousto-optic modulators, and quantum transducers [6].

Strain permits tailoring the electronic and optical landscapes of two-dimensional (2D) materials [7–11] by inducing gauge fields [12], shifting excitonic emission energies [13, 14], and enhancing electron mobility [15, 16]. However, despite the extensive study of intralayer responses, the optomechanics of the interlayer van der Waals (vdW) coupling has only begun to be explored [17]. When strain is created in-plane, a fundamental question is the extent to which the mechanical deformation within the plane propagates across monolayers (MLs).

Understanding this cross-coupling is critical for designing vdW heterostructures, where the subtle interplay between MLs dictates phenomena ranging from moiré excitons and hyperlubricity to superconductivity and topological phases [18–21]. In this direction, Du and coworkers studied few-ML MoS<sub>2</sub> under isotropic compressive strain [17]. Here, we instead consider anisotropic coupling between in-plane and out-of-plane strain.

We synthesized MoS<sub>2</sub> BLs under biaxial tensile strain [22] on SiO<sub>2</sub> [Fig. 1(a)] and Si<sub>3</sub>N<sub>4</sub> substrates (see Supplemental Material [23]); MLs develop triangular shapes. Bilayer flakes are created by the successive growth of triangular MLs; smaller triangles around the centers of larger ones in Fig. 1(a) are showcased within white dashed lines. The top ML shows different orientations depending on the BL phase: it rotates by 60° relative to the lower ML in the 2H phase, but it forms a concentric structure with parallel edges in the 2R BL [28]. Our first-principles calculations show an energy difference of only  $\sim 0.7$  meV per unit cell between the two phases [23], resulting in a similar likelihood for either configuration

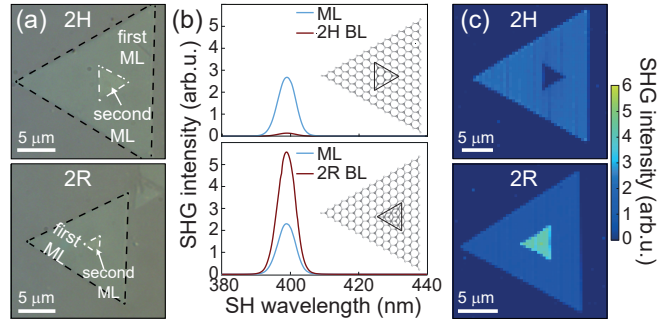


FIG. 1. (a) Optical contrast images of 2H and 2R MoS<sub>2</sub> BLs grown on a SiO<sub>2</sub> substrate. (b) SHG spectra for monolayer, 2H and 2R bilayers. Insets are ball and stick models. (c) SHG intensity maps in monolayer and BL regions.

to be created.

A single-location SHG spectrum within ML sections is displayed in blue on Fig. 1(b); peaks are centered at half the wavelength of the incident laser. Due to its center of inversion, the nominal SHG from a 2H BL is zero; the small nonzero SHG intensity seen in top panel is likely due to a small breaking of inversion symmetry with an air-material-substrate structure. In contrast, the SHG signal on the 2R BL (dark red curve in the bottom panel) is more than twice that of the ML one. Chalcogen atoms form zigzag edges, and the edge conformation of 2H and 2R BLs was recreated with ball-and-stick models in the insets of Fig. 1(b). The presence of a center of inversion was spatially probed by SHG in Fig. 1(c) [23], which greatly increases the contrast of both 2H and 2R BL sections when compared to that obtained with an optical microscope [Fig. 1(a)].

The response of high-frequency—in-plane  $E_{2g}^1$  and out-of-plane  $A_{1g}$  vibrations—Raman intralayer modes is the primary gauge for quantifying isotropic pressure [17] and strain [22, 29–32] in layered materials. While uniaxial strain breaks hexagonal symmetry and splits the  $E_{2g}^1$  degeneracy [33], biaxial strain preserves that symmetry,

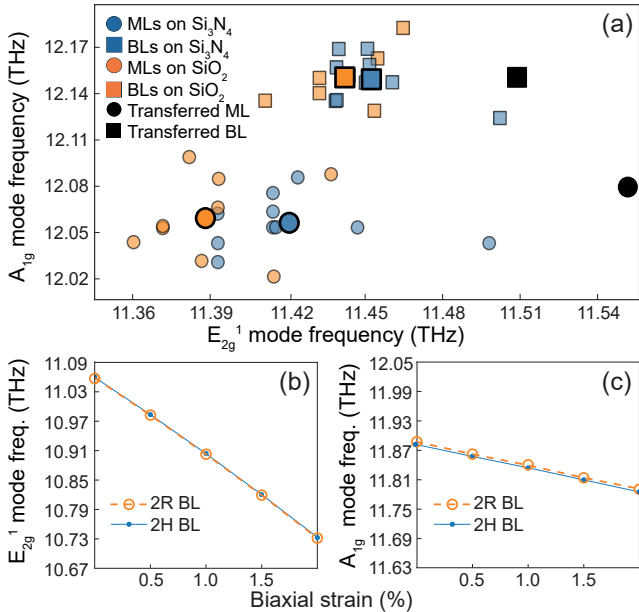


FIG. 2. (a) Correlation between  $A_{1g}$  and  $E_{2g}^1$  peak positions for MLs (small circles) and 2H BLs (small squares), including average values (large circles and squares). The black circle (square) corresponds to samples where the strain was released after transferring a MoS<sub>2</sub> ML (BL) onto another SiO<sub>2</sub> substrate. (b)  $E_{2g}^1$  and (c)  $A_{1g}$  mode frequencies from DFT calculations for 2H (orange) and 2R (light blue) phases, respectively. Both modes red-shift under in-plane biaxial strain.

leading to a systematic redshift of the  $E_{2g}^1$  mode with increasing tension [30].

Biaxial strain is determined from the thermal expansion mismatch between the TMDC and the growth substrate [22, 34], estimated as Strain(%) =  $(\alpha_{MoS_2} - \alpha_{sub}) \Delta T \times 100$ , where  $\alpha$  denotes the thermal expansion coefficients and  $\Delta T$  is the difference between growth ( $T_{growth}$ ) and room ( $T_{room}$ ) temperatures. Therefore, our MoS<sub>2</sub> samples are subjected to a tensile strain of +0.36% on  $Si_3N_4$  and +0.72% on  $SiO_2$  [23].

The substrate-dependent evolution of the  $A_{1g}$  and  $E_{2g}^1$  modes for MoS<sub>2</sub> MLs (circles) and BLs (squares) is shown in Fig. 2(a). Frequencies of individual flakes appear in lighter-colored symbols, from which average values (larger, opaque symbols) were obtained. With average values of 12.05 THz and 12.14 THz for MLs and BLs, the  $A_{1g}$  mode has negligible substrate dependence [23]. In contrast, the  $E_{2g}^1$  mode redshifts, reflecting a greater tensile strain when on  $SiO_2$  than on  $Si_3N_4$  [23].

Frequency renormalization (and hence tensile strain) is further evidenced by comparison with control MoS<sub>2</sub> ML and BL samples transferred onto  $SiO_2/Si$ , for which the growth-induced strain is released (see Section S6 and Fig. S4 [23]). In the relaxed control sample, the  $E_{2g}^1$  mode blueshifts by 0.16 THz (0.06 THz) for ML (BL), relative to the as-grown samples on  $SiO_2$ , while the  $A_{1g}$  mode shifts by only  $\sim 0.03$  THz [Fig. 2(a)]. These trends

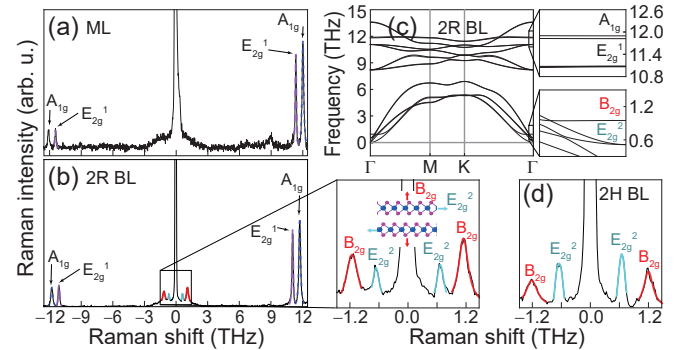


FIG. 3. (a) Raman spectrum of a MoS<sub>2</sub> ML on  $SiO_2$ . (b) Raman spectrum of a 2R BL on  $SiO_2$ ; the magnified view between  $-1.5$  and  $1.5$  THz shows signatures of shear ( $E_{2g}^2$ ) and breathing ( $B_{2g}$ ) modes absent in the monolayer. (c) Strain-free phonon dispersion for a 2R bilayer. Raman-active high- and low-frequency modes are highlighted on insets. (d) Low-frequency Raman spectrum of 2H phase on  $SiO_2$ .

are reproduced by calculations [Figs. 2(b,c)], where the sensitivity of the  $E_{2g}^1$  mode to strain is found to be about three times that of the  $A_{1g}$  mode. Using the measured frequency difference between as-grown and strain-released 2H-BLs, we extract a strain-tuning rate (strain-induced red shift) for the *intralayer*  $E_{2g}^1$  mode equal to  $-0.10$  THz/% which aligns with our theoretical estimate of  $-0.15$  THz/% reasonably well. Fig. 3(a) is a sample, individual Raman spectrum contributing to the ML statistics on Fig. 2(a).

While high-energy phonons map the in-plane stress field, they offer limited insight into the evolution of the interlayer coupling itself, and we next turn to the low-frequency Raman spectra near 1 THz in Fig. 3(b)—where the rigid-layer Shear ( $E_{2g}^2$ ) and Breathing ( $B_{2g}$ ) modes reside—to probe the vertical interaction among MLs. Phonon dispersions for strain-free 2R [Fig. 3(c)] and 2H [23] BLs were calculated as well.

The mechanical response of interlayer modes to strain is not completely understood. Previous work showed uniaxial strain splitting the degenerate  $E_{2g}^2$  modes [35], yet the behavior of the  $B_{2g}$  mode—which corresponds to the out-of-plane oscillation and is a direct proxy for the interlayer distance—was studied under hydrostatic compressive strain [17]; not biaxial tensile strain.

The zoom-in on Fig. 3(c) and Fig. 3(d) contrast low-frequency spectra for the 2H and 2R BLs, respectively. The Raman amplitude of the  $E_{2g}^2$  mode (0.67 THz) exceeds that of the  $B_{2g}$  mode (1.20 THz) in the 2H BL (see Ref. [23], too). In contrast, this intensity ratio is inverted in the 2R BL, where the  $B_{2g}$  mode has a larger amplitude. This reversal in amplitude reflects the different symmetries of the two stacking orders. The  $E_{2g}^2$ -mode degeneracy, protected by the  $C_3$  symmetry of the hexagonal lattice, serves as a sensitive probe for symmetry-breaking perturbations such as uniaxial strain [35]. The

lack of  $E_{2g}^2$ -mode splitting in our BL samples, as well as the isotropic intensity for the polarization-resolved SHG of 2R-MoS<sub>2</sub> BL (Fig. S6 [23]), are both consistent with the uniform, biaxial nature of strain [22, 36].

We next correlate the response of the interlayer coupling to the strain created during growth. We display the measured low-frequency modes for 2H [Figs. 4(a,b)] and 2R (Fig. S7 [23]) BLs on both growth substrates. We include 2H BL samples for which strain was released by transferring the BL onto a SiO<sub>2</sub> substrate [23]. The  $E_{2g}^2$  mode undergoes a slight blueshift under tensile strain [Fig. 4(b); and Ref. [23]]. However, the most striking feature is the response of the  $B_{2g}$  mode, which *undergoes a significant hardening with increasing strain*: the average  $B_{2g}$ -mode frequency increases from 1.13 THz (0% strain; transferred) to 1.19 THz (+0.72% strain; SiO<sub>2</sub>), yielding a substantial experimental strain-tuning rate of +0.07 THz/%. Thus, we have demonstrated that biaxial strain created by growth can be used in lieu of isotropic strain to tune the optomechanical response of MoS<sub>2</sub> BLs at the application-relevant  $\sim 1$  THz oscillator range. This response remains in place as strain is built-in during growth.

This hardening of the out-of-plane vibration under in-plane tension is counter-intuitive for standard harmonic oscillators and it arises from the Poisson effect. As the MoS<sub>2</sub> BL is stretched biaxially, the interlayer spacing contracts to conserve volume, steepening the confinement potential. We corroborate this mechanism using first-principles calculations, which reproduce the monotonic hardening of the  $B_{2g}$  mode [Fig. 4(c)] and confirm the reduction in ML spacing  $d$  [Fig. 4(d)].

The interlayer phonon frequencies and their renormalization due to strain are sensitive to the approximation for the vdW interaction used in calculations [23]. However, the Poisson compression (vertical contraction,  $\Delta d$ ) driving the  $B_{2g}$ -mode hardening was robust irrespective of exchange-correlation functional. We also note that while the theory captures the qualitative trend, the predicted magnitude of the shift ( $\sim 0.01$  THz/%) is significantly smaller than in experiments. This quantitative discrepancy highlights the difficulty standard functionals have in fully capturing the strain-sensitivity of the vdW potential anharmonicity. Nevertheless, the geometric response—the vertical contraction of the layer spacing—is robust across different functionals (see Fig. S2 [23]).

We rely on a geometric response to quantify the effective Poisson's ratio ( $\nu_{\text{eff}}$ ) of BLs. Using the relation for isotropic biaxial strain assuming the BL behaves as a continuum elastic medium [23, 37]:

$$\nu_{\text{eff}} = \frac{-\varepsilon_{\perp}/\varepsilon_{\parallel}}{2 - \varepsilon_{\perp}/\varepsilon_{\parallel}}, \quad (1)$$

where  $\varepsilon_{\parallel}$  is the applied in-plane strain and  $\varepsilon_{\perp}$  is the induced vertical strain derived from the theoretical van

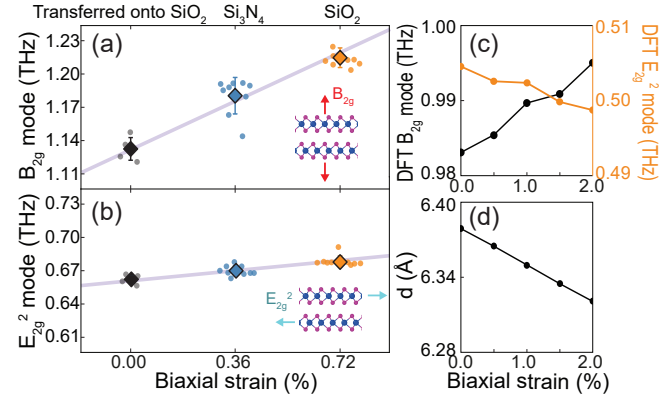


FIG. 4. Experimental evolution of the (a)  $B_{2g}$  and (b)  $E_{2g}^2$  frequencies for 2H-stacked MoS<sub>2</sub> BLs under varying biaxial tensile strain. (c) DFT calculations of the breathing (black) and shear (orange) mode frequencies for 2H MoS<sub>2</sub>. (d) Interlayer distance  $d$  vs. in-plane biaxial strain.

TABLE I. Poisson's ratios ( $\nu$ ) for representative 3D semiconductors, perovskite oxides, and layered materials. The value for the MoS<sub>2</sub> BL is estimated using  $d$  [Fig. 4(d)].

Material Class	Material	Poisson's Ratio ( $\nu$ )	Ref.
Group IV	Silicon (Si)	0.28	[40]
	Germanium (Ge)	0.27	[40]
III-V	GaAs	0.31	[41]
Perovskite	SrTiO <sub>3</sub>	0.25	[42]
	BaTiO <sub>3</sub>	0.31	[43]
Layered	Graphite ( $\nu_{\text{out}}$ )	0.29	[44]
Layered TMDs	MoS <sub>2</sub> (Bulk, Exp.)	$\sim 0.30$	[38]
	MoS <sub>2</sub> (Bulk, Theo.)	$\sim 0.17$	[39]
<b>this work</b>	<b>MoS<sub>2</sub> BL</b>	<b>0.19-0.24</b>	—

der Waals gap contraction shown in Figure 4d. This calculation yields  $\nu_{\text{eff}} = 0.19 - 0.24$ , depending on the exchange-correlation approximation. As shown in Table I, this value is notably lower than those reported for other three-dimensional materials as well as for bulk MoS<sub>2</sub> ( $\nu_{\text{eff}} \approx 0.30$ ) [38]. We note that the literature value for bulk MoS<sub>2</sub> was derived indirectly from linear compressibility measurements, while theoretical estimates for the relevant elastic constant ( $C_{13}$ ) have shown significant scatter (3–39 GPa) depending on the treatment of vdW interactions [39]. Our result aligns closely with modern hybrid-functional DFT (HSE06-D2) results, which predicts a lower bulk Poisson's ratio of  $\nu_{\text{eff}} \approx 0.17$  [39].

One notable discrepancy between the experiment and DFT results is how much the interlayer phonon hardens in response to the Poisson compression, which can be described by the Grüneisen parameter. To the best of our knowledge, the Grüneisen parameter for the interlayer breathing mode in a few-ML transition metal dichalcogenides (TMDs) has not been previously determined

experimentally. While intralayer modes ( $E_{2g}^1$ ,  $A_{1g}$ ) in MoS<sub>2</sub>, MoSe<sub>2</sub>, and WSe<sub>2</sub> typically exhibit Grüneisen parameters near unity ( $\gamma \approx 1$ ) [45, 46], our measurement yields a significantly larger value. We estimate the out-of-plane Grüneisen parameter ( $\gamma_{out}$ ) using the definition:

$$\gamma_{out} = -\frac{1}{\omega_0} \frac{\partial \omega}{\partial \varepsilon_{\perp}}, \quad (2)$$

where  $\omega_0$  is the zero-strain frequency (1.13 THz) and  $\partial \omega / \partial \varepsilon_{\perp}$  is the rate of frequency shift with respect to vertical strain. By combining our experimental tuning rate ( $\partial \omega / \partial \varepsilon_{\parallel} \approx 0.07$  THz/%) with the theoretical Poisson contraction ratio ( $\varepsilon_{\perp} / \varepsilon_{\parallel} \approx -0.47$  to  $-0.65$ ), we obtain  $\gamma_{out} \approx 10\text{--}14$ . This value exceeds even the ‘giant’  $\gamma$  reported for phosphorene ( $\gamma \approx 8.6$ ) [47], highlighting the extreme sensitivity of the curvature of vdW potential to the geometrical compression.

Our findings redefine the van der Waals spacing in BL systems as a dynamic, highly tunable degree of freedom at the THz oscillation regime. We established that the soft vertical coupling acts as a sensitive amplifier of in-plane mechanical deformation. The resulting stiffening of the interlayer bond implies a direct modulation of the electronic interlayer hopping parameter ( $t_{\perp}$ ). This electromechanical coupling provides a physical basis for dynamically manipulating the layer hybridization of excitons, thereby controlling their lifetimes and valley coherence [48, 49]. Furthermore, as the field advances toward twisted heterostructures, this effect offers a deterministic knob to tune the bandwidth of moiré flatbands without changing the twist angle [50, 51], paving the way for strain-tunable correlated phases and optomechanics.

We thank R. Rodriguez, M. Marking, K. Reynolds, H. Churchill, and P. Kumar. This work is supported by the Office of the Secretary of Defense for Research and Engineering (Award No. FA9550-23-1-0500) and the NSF’s Q-AMASE-i program (Award No. DMR-1906383). Calculations were performed at the Arkansas HPCC (NSF Award No. OAC-2346752).

sponse generated in graphene/MoS<sub>2</sub> heterostructures, *Adv. Mater.* **37**, 2503590 (2025).

- [5] C. A. Bhuyan, A. K. Chaudhary, K. K. Madapu, P. N. Kumar, and S. Dhara, Enhanced THz emission and exciton transfer in monolayer MoS<sub>2</sub>/GaAs heterostructures, *Adv. Photon. Res.* **7**, e202500153 (2026).
- [6] Y. Yoon, Z. Lu, C. Uzundal, R. Qi, W. Zhao, S. Chen, Q. Feng, W. Kim, M. H. Naik, K. Watanabe, T. Taniguchi, S. G. Louie, M. F. Crommie, and F. Wang, Terahertz phonon engineering with van der Waals heterostructures, *Nature* **631**, 771 (2024).
- [7] R. Roldán, A. Castellanos-Gómez, E. Cappelluti, and F. Guinea, Strain engineering in semiconducting two-dimensional crystals, *J. Phys.: Condens. Matter* **27**, 313201 (2015).
- [8] B. Amorim, A. Cortijo, F. De Juan, A. Grushin, F. Guinea, A. Gutiérrez-Rubio, H. Ochoa, V. Parente, R. Roldán, P. San-Jose, J. Schiefele, M. Sturla, and M. Vozmediano, Novel effects of strains in graphene and other two dimensional materials, *Phys. Rep.* **617**, 1 (2016).
- [9] G. G. Naumis, S. Barraza-Lopez, M. Oliva-Leyva, and H. Terrones, Electronic and optical properties of strained graphene and other strained 2D materials: a review, *Rep. Prog. Phys.* **80**, 096501 (2017).
- [10] Z. Peng, X. Chen, Y. Fan, D. J. Srolovitz, and D. Lei, Strain engineering of 2D semiconductors and graphene: from strain fields to band-structure tuning and photonic applications, *Light Sci. Appl.* **9**, 190 (2020).
- [11] G. G. Naumis, S. A. Herrera, S. P. Poudel, H. Nakamura, and S. Barraza-Lopez, Mechanical, electronic, optical, piezoelectric and ferroic properties of strained graphene and other strained monolayers and multilayers: an update, *Rep. Prog. Phys.* **87**, 016502 (2024).
- [12] A. A. Pacheco Sanjuan, Z. Wang, H. P. Imani, M. Vanević, and S. Barraza-Lopez, Graphene’s morphology and electronic properties from discrete differential geometry, *Phys. Rev. B* **89**, 121403 (2014).
- [13] H. J. Conley, B. Wang, J. I. Ziegler, R. F. Haglund, S. T. Pantelides, and K. I. Bolotin, Bandgap engineering of strained monolayer and bilayer MoS<sub>2</sub>, *Nano Lett.* **13**, 3626 (2013).
- [14] X. He, H. Li, Z. Zhu, Z. Dai, Y. Yang, P. Yang, Q. Zhang, P. Li, U. Schwingenschlögl, and X. Zhang, Strain engineering in monolayer WS<sub>2</sub>, MoS<sub>2</sub>, and the WS<sub>2</sub>/MoS<sub>2</sub> heterostructure, *Appl. Phys. Lett.* **109**, 173105 (2016).
- [15] J. A. Yang, R. K. A. Bennett, L. Hoang, Z. Zhang, K. J. Thompson, A. Michail, J. Parthenios, K. Papagelis, A. J. Mannix, and E. Pop, Biaxial tensile strain enhances electron mobility of monolayer transition metal dichalcogenides, *ACS Nano* **18**, 18151 (2024).
- [16] I. M. Datye, A. Daus, R. W. Grady, K. Brenner, S. Vaziri, and E. Pop, Strain-enhanced mobility of monolayer MoS<sub>2</sub>, *Nano Lett.* **22**, 8052 (2022).
- [17] G. Du, L. Zhao, S. Li, J. Huang, S. Fang, W. Han, J. Li, Y. Du, J. Ming, T. Zhang, J. Zhang, J. Kang, X. Li, W. Xu, and Y. Chen, Interlayer engineering of lattice dynamics and elastic constants of 2D layered nanomaterials under pressure, *Nat. Commun.* **16**, 4901 (2025).
- [18] Z. Bian, J. Miao, Y. Zhao, and Y. Chai, Strong interlayer interaction for engineering two-dimensional materials, *Acc. Mater. Res.* **3**, 1220 (2022).
- [19] K. Tran, G. Moody, F. Wu, X. Lu, J. Choi, K. Kim, A. Rai, D. A. Sanchez, J. Quan, A. Singh, J. Emb

\* hnakamur@uark.edu

- [1] A. Leitenstorfer, et al., The 2023 terahertz science and technology roadmap, *J. Phys. D: Appl. Phys.* **56**, 10.1088/1361-6463/acbe4c.
- [2] D. Pavlidis, ed., *Fundamentals of Terahertz Devices and Applications*, 1st ed. (John Wiley and Sons, New Jersey, 2021).
- [3] M. A. Lund, D. R. Rodrigues, K. Everschor-Sitte, and K. M. Hals, Voltage-controlled high-bandwidth terahertz oscillators based on antiferromagnets, *Phys. Rev. Lett.* **131**, 156704 (2023).
- [4] S. Sharma, D. P. Singh, S. Rane, S. Srivastava, A. B. Puthirath, R. Puranik, U. Pandey, S. Haldankar, V. Parkar, F. Faseela, et al., Probing into intraband transitions enabled charge carrier dynamics of thz re

ley, A. Zepeda, M. Campbell, T. Autry, T. Taniguchi, K. Watanabe, N. Lu, S. K. Banerjee, K. L. Silverman, S. Kim, E. Tutuc, L. Yang, A. H. MacDonald, and X. Li, Evidence for moiré excitons in van der Waals heterostructures, *Nature* **567**, 71 (2019).

[20] Y. Cao, V. Fatemi, S. Fang, K. Watanabe, T. Taniguchi, E. Kaxiras, and P. Jarillo-Herrero, Unconventional superconductivity in magic-angle graphene superlattices, *Nature* **556**, 43 (2018).

[21] A. L. Sharpe, E. J. Fox, A. W. Barnard, J. Finney, K. Watanabe, T. Taniguchi, M. A. Kastner, and D. Goldhaber-Gordon, Emergent ferromagnetism near three-quarters filling in twisted bilayer graphene, *Science* **365**, 605 (2019).

[22] S. Patel, T. Faltermeier, S. Puri, R. Rodriguez, K. Reynolds, S. Davari, C. McPherson, H. O. H. Churchill, N. J. Borys, and H. Nakamura, Biaxial strain tuning of excitons in monolayer MoSe<sub>2</sub> by high-temperature physical vapor deposition, *Phys. Rev. B* **110**, 245310 (2024).

[23] See Supplemental Material at <http://link.aps.org/supplemental/xxxx/xxxx> for details of the growth of MoS<sub>2</sub> bilayers, *ab-initio* calculations, Raman and SHG spectroscopies, estimation of strain due to thermal expansion mismatch, substrate-dependent high frequency Raman modes on 2H-MoS<sub>2</sub> bilayers, the transfer process of PVD-ground MoS<sub>2</sub>, Raman spectra of shear and breathing modes of 2H-MoS<sub>2</sub> bilayers on both substrates, polarization-resolved SHG of 2R-MoS<sub>2</sub>, strain evolution of interlayer vibration in 2R-MoS<sub>2</sub>, Raman spectrum of 2H-MoS<sub>2</sub> as-grown on SiO<sub>2</sub> and when is transferred, the derivation of effective poisson's ratio, and estimation of the vertical strain ratio, which includes Refs. [24-27].

[24] G. Kresse and J. Furthmüller, Efficiency of ab-initio total energy calculations for metals and semiconductors using a plane-wave basis set, *Comput. Mater. Sci.* **6**, 15 (1996).

[25] J. Klimeš, D. R. Bowler, and A. Michaelides, Chemical accuracy for the van der Waals density functional, *J. Phys.: Condens. Matter* **22**, 022201 (2010).

[26] J. P. Perdew, K. Burke, and M. Ernzerhof, Generalized Gradient Approximation Made Simple, *Phys. Rev. Lett.* **77**, 3865–3868 (1996).

[27] S. Grimme, J. Antony, S. Ehrlich, and H. Krieg, A consistent and accurate *ab initio* parametrization of density functional dispersion correction (DFT-D) for the 94 elements H–Pu, *J. Chem. Phys.* **132**, 154104 (2010).

[28] J. M. Marmolejo-Tejada, J. E. Roll, S. P. Poudel, S. Barraza-Lopez, and M. A. Mosquera, Slippery paraelectric transition-metal dichalcogenide bilayers, *Nano Lett.* **22**, 7984 (2022).

[29] B. Chakraborty, A. Bera, D. V. S. Muthu, S. Bhowmick, U. V. Waghmare, and A. K. Sood, Symmetry-dependent phonon renormalization in monolayer MoS<sub>2</sub> transistor, *Phys. Rev. B* **85**, 161403 (2012).

[30] D. Lloyd, X. Liu, J. W. Christopher, L. Cantley, A. Wadehra, B. L. Kim, B. B. Goldberg, A. K. Swan, and J. S. Bunch, Band gap engineering with ultralarge biaxial strains in suspended monolayer MoS<sub>2</sub>, *Nano Lett.* **16**, 5836 (2016).

[31] R. Rao, A. E. Islam, S. Singh, R. Berry, R. K. Kawakami, B. Maruyama, and J. Katoch, Spectroscopic evaluation of charge-transfer doping and strain in graphene/MoS<sub>2</sub> heterostructures, *Phys. Rev. B* **99**, 195401 (2019).

[32] R. N. Gontijo, N. Bunker, S. L. Graiser, X. Ding, M. Smeu, and A. L. Elías, Resonant raman scattering study of strain and defects in chemical vapor deposition grown MoS<sub>2</sub> monolayers, *Small* **21**, 2310685 (2025).

[33] Y. Wang, C. Cong, C. Qiu, and T. Yu, Raman spectroscopy study of lattice vibration and crystallographic orientation of monolayer MoS<sub>2</sub> under uniaxial strain, *Small* **9**, 2857 (2013).

[34] G. H. Ahn, M. Amani, H. Rasool, D.-H. Lien, J. P. Mastandrea, J. W. Ager III, M. Dubey, D. C. Chrzan, A. M. Minor, and A. Javey, Strain-engineered growth of two-dimensional materials, *Nat. Commun.* **8**, 608 (2017).

[35] J.-U. Lee, S. Woo, J. Park, H. C. Park, Y.-W. Son, and H. Cheong, Strain-shear coupling in bilayer MoS<sub>2</sub>, *Nat. Commun.* **8**, 1370 (2017).

[36] S. Puri, S. Patel, J. L. Cabellos, L. E. Rosas-Hernandez, K. Reynolds, H. O. H. Churchill, S. Barraza-Lopez, B. S. Mendoza, and H. Nakamura, Substrate interference and strain in the second-harmonic generation from MoSe<sub>2</sub> monolayers, *Nano Lett.* **24**, 13061 (2024).

[37] L. D. Landau and E. M. Lifshitz, *Theory of Elasticity*, 3rd ed. (Pergamon Press, Oxford, 1986).

[38] J. Feldman, Elastic constants of 2H-MoS<sub>2</sub> and 2H-NbSe<sub>2</sub> extracted from measured dispersion curves and linear compressibilities, *J. Phys. Chem. Solids* **37**, 1141 (1976).

[39] H. Peelaers and C. G. Van De Walle, Elastic constants and pressure-induced effects in MoS<sub>2</sub>, *J. Phys. Chem. C* **118**, 12073 (2014).

[40] J. J. Wortman and R. A. Evans, Young's modulus, shear modulus, and poisson's ratio in silicon and germanium, *J. Appl. Phys.* **36**, 153 (1965).

[41] J. S. Blakemore, Semiconducting and other major properties of gallium arsenide, *J. Appl. Phys.* **53**, R123 (1982).

[42] R. O. Bell and G. Rupprecht, Elastic constants of strontium titanate, *Phys. Rev.* **129**, 90 (1963).

[43] D. Berlincourt and H. Jaffe, Elastic and piezoelectric coefficients of single-crystal barium titanate, *Phys. Rev.* **111**, 143 (1958).

[44] O. L. Blakslee, D. G. Proctor, E. J. Seldin, G. B. Spence, and T. Weng, Elastic constants of compression-annealed pyrolytic graphite, *J. Appl. Phys.* **41**, 3373 (1970).

[45] A. M. Dadgar, D. Scullion, K. Kang, D. Esposito, E. H. Yang, I. P. Herman, M. A. Pimenta, E.-J. G. Santos, and A. N. Pasupathy, Strain engineering and raman spectroscopy of monolayer transition metal dichalcogenides, *Chem. Mater.* **30**, 5148 (2018).

[46] S. Huang, L. Liang, X. Ling, A. A. Puretzky, D. B. Geoghegan, B. G. Sumpter, J. Kong, V. Meunier, and M. S. Dresselhaus, Low-frequency interlayer raman modes to probe interface of twisted bilayer MoS<sub>2</sub>, *Nano Lett.* **16**, 1435 (2016).

[47] Y. Cai, Q. Ke, G. Zhang, Y. P. Feng, V. B. Shenoy, and Y. Zhang, Giant Phononic Anisotropy and Unusual Anharmonicity of Phosphorene: Interlayer Coupling and Strain Engineering, *Adv. Funct. Mater.* **25**, 22230 (2015).

[48] E. M. Alexeev, D. A. Ruiz-Tijerina, M. Danovich, M. J. Hamer, D. J. Terry, P. K. Nayak, S. Ahn, S. Pak, J. Lee, J. I. Sohn, M. R. Molas, M. Koperski, K. Watanabe, T. Taniguchi, K. S. Novoselov, R. V. Gorbachev, H. S. Shin, V. I. Fal'ko, and A. I. Tartakovskii, Resonantly hybridized excitons in moiré superlattices in van der Waals heterostructures, *Nature* **567**, 81 (2019).

[49] P. Rivera, H. Yu, K. L. Seyler, N. P. Wilson, W. Yao, and X. Xu, Interlayer valley excitons in heterobilayers of

transition metal dichalcogenides, *Nat. Nanotechnol.* **13**, 1004 (2018).

[50] Z. Bi, N. F. Q. Yuan, and L. Fu, Designing flat bands by strain, *Phys. Rev. B* **100**, 035448 (2019).

[51] S. Li, X. Shi, J. Li, C. He, T. Ouyang, C. Tang, and J. Zhong, Strain-induced flatbands in large-angle twisted bilayer graphene, *J. Appl. Phys.* **137**, 083902 (2025).

**Supplemental Material for**  
**Tuning Terahertz Optomechanics of MoS<sub>2</sub> Bilayers**  
**with Homogeneous In-plane Strain**

S. Patel<sup>1</sup>, Jose D. Mella<sup>1</sup>, S. Puri<sup>1</sup>, Salvador Barraza-Lopez<sup>1,2</sup>, H. Nakamura<sup>1</sup>

<sup>1</sup>*Department of Physics, University of Arkansas, Fayetteville, AR 72701, USA*

<sup>2</sup>*Institute for Solid State Physics, University of Tokyo, Kashiwa, 277-8581, Chiba, Japan*

**S1. GROWTH OF MOS<sub>2</sub> BILAYERS**

MoS<sub>2</sub> bilayer films were grown using a home-built physical vapor deposition (PVD) system at a growth temperature of 1200°C using pure MoS<sub>2</sub> powder as source material [1]. The high growth temperature enables application of a large tensile strain originating from thermal expansion mismatch between amorphous substrates and grown 2D materials [1]. The PVD system is equipped with two mass flow controllers installed on both sides of a quartz tube (diameter 1 inch) that regulate the Ar flow to prevent unwanted deposition. Following a growth time of 5-10 seconds, we rapidly quenched the temperature by sliding the furnace away from the location of the powder and the substrate. Substrates were silicon with custom-grown oxide or nitride layers of 90 nm (SiO<sub>2</sub>) and 70 nm (Si<sub>3</sub>N<sub>4</sub>) in thickness, optimized to enhance the optical contrast of grown flakes.

**S2. AB INITIO CALCULATIONS**

DFT calculations were performed with the *Vienna Ab Initio Simulation Package* (VASP) [2]. The calculations were carried out using PAW pseudopotentials and optPBE-vdW density functional [3]. Figure S2 contains results obtained from PBE exchange-correlation functional combined with the empirical vdW correction proposed by Grimme *et al.* [4, 5] (DFT-D3) with zero-damping function. We used a 18×18×1 *k*-point mesh, an energy cutoff of 400 eV, and an electronic energy convergence criteria of 10<sup>-8</sup> eV. A force convergence of 10<sup>-6</sup> eV/Å was set for structural relaxations. All calculations were performed with an out-of-plane lattice constant of  $c \sim 60$  Å to reduce self-interaction among periodic copies. The energy difference between the 2H and 2R phases after structural relaxation is 0.7 meV. The applied strain to the system as  $a = a_0(1 + \varepsilon)$ , where  $a$  and  $a_0$  denote the lattice parameter with and without strain and  $\varepsilon$  the strain. To apply strain to the system, the lattice parameter was modified by a desired percentage, and then the atomic positions were relaxed while keeping the lattice vectors fixed. The distance between monolayers was defined as  $z_1 - z_2$ , where  $z_1, z_2$  denote the geometric centers of the top and bottom monolayers, respectively. Phonons were calculated within the harmonic approximation using the Phonopy package [6, 7] after full structural relaxation at each value of strain. The phonon dispersion was calculated for a 5×5×1 supercell with a displacement of 0.05 Å and a 3×3×1 *k*-point mesh. For the optPBE-vdW density functional, the lattice parameter is 3.20 Å for both 2H and 2R phases. The monolayer thickness, defined as the out-of-plane S–S distance within a single MoS<sub>2</sub> monolayer, is 3.15 Å for both stacking configurations. The equilibrium interlayer sulfur distance is 3.23 Å for 2H and 3.22 Å for the 3R structure.

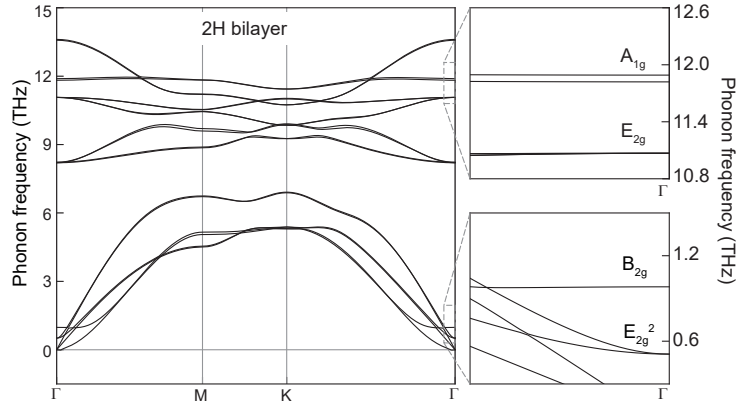


FIG. S1. Phonon dispersion of a strain-free 2H-MoS<sub>2</sub> bilayer. The low and high frequency modes near  $\Gamma$  are highlighted in the two panels on the right.

The phonon dispersions for the unstrained 2H and 3R phases are shown in Fig. 3(c) of the main text and Fig. S1, respectively, while the strain response of the vibrational modes is shown in Fig. 2(b,c) and Fig. 4(c,d) of the main text, as well as Fig. S7(c,d). For comparison, we include vdW effects through DFT-D3 corrections within the PBE functional (*i.e.*, setting IVDW = 11 as an input). The lattice parameters used were 3.16 Å and 3.17 Å for the 2H and 3R phases, respectively. The monolayer thickness is 3.13 Å for both phases, and the interlayer sulfur distance is 3.06 Å (2H) and 3.05 Å (3R). Figure S2 summarizes the phonon properties of 2H and 2R within this approximation. Although the numerical values differ between the two approximations, they describe the same qualitative trends.

### S3. RAMAN AND SHG SPECTROSCOPIES

Raman measurements were carried out using a home-built system equipped with a 532 nm excitation laser. An objective lens with 50× (NA = 0.55) magnification was used to focus the light on the sample, and the laser power on the sample was below 2 mW. We used two narrow-line OD4 Bragg type filters (Optigate) to reject the laser line, which allowed us to measure Raman shifts down to  $\sim$ 20 cm<sup>-1</sup> for both Stokes and anti-Stokes peaks. The Raman peaks from the silicon substrate were used to calibrate the Raman shifts.

The detail of the second harmonic generation (SHG) setup is reported elsewhere [8]. Briefly, Ti:sapphire fs oscillator (Tsunami, Spectra-Physics) with an 80 MHz repetition frequency was used as an excitation laser, which delivered a temporal pulse width of  $\sim$ 100 fs with  $\sim$ 1 mW at the position of the sample. The reflected SHG was observed through filters that rejected the fundamental beam, and the angular dependence was taken by rotating the sample. Motorized XY stages allowed a spatially resolved SHG mapping by translating the sample. All Raman and SHG measurements were performed in air at room temperature.

### S4. ESTIMATION OF STRAIN DUE TO THERMAL EXPANSION MISMATCH

The biaxial strain induced due to mismatch in the thermal expansion coefficients of the transition metal dichalcogenide (TMD) bilayer and the underlying substrate is given by [1, 9]:

$$\% \text{ strain} = (\alpha_{\text{TMD}} - \alpha_{\text{sub}}) \cdot \Delta T \cdot 100, \quad (\text{S1})$$

where  $\alpha_{\text{TMD}}$  is the thermal expansion coefficient of MoS<sub>2</sub>,  $\alpha_{\text{sub}}$  is that of Si<sub>3</sub>N<sub>4</sub> or SiO<sub>2</sub>, and  $\Delta T = T_{\text{growth}} - T_{\text{room}}$ . This expression provides an approximate estimate because it uses average (constant) thermal expansion coefficients over the relevant temperature range. We employed the following values:  $\alpha_{\text{MoS}_2} = 6.6 \times 10^{-6} \text{ K}^{-1}$  [10],  $\alpha_{\text{SiO}_2} = 5.0 \times 10^{-7} \text{ K}^{-1}$  [11], and  $\alpha_{\text{Si}_3\text{N}_4} = 3.5 \times 10^{-6} \text{ K}^{-1}$  [12]. Using  $T_{\text{room}} = 25^\circ\text{C}$  and  $T_{\text{growth}} = 1200^\circ\text{C}$ , we estimate tensile strains of +0.36% for MoS<sub>2</sub> on Si<sub>3</sub>N<sub>4</sub>, and +0.72% for MoS<sub>2</sub> on SiO<sub>2</sub>. These results indicate that thermal-expansion mismatch can induce substantial tensile strain in TMD films grown at elevated temperatures, with the largest effects occurring on SiO<sub>2</sub> substrates.

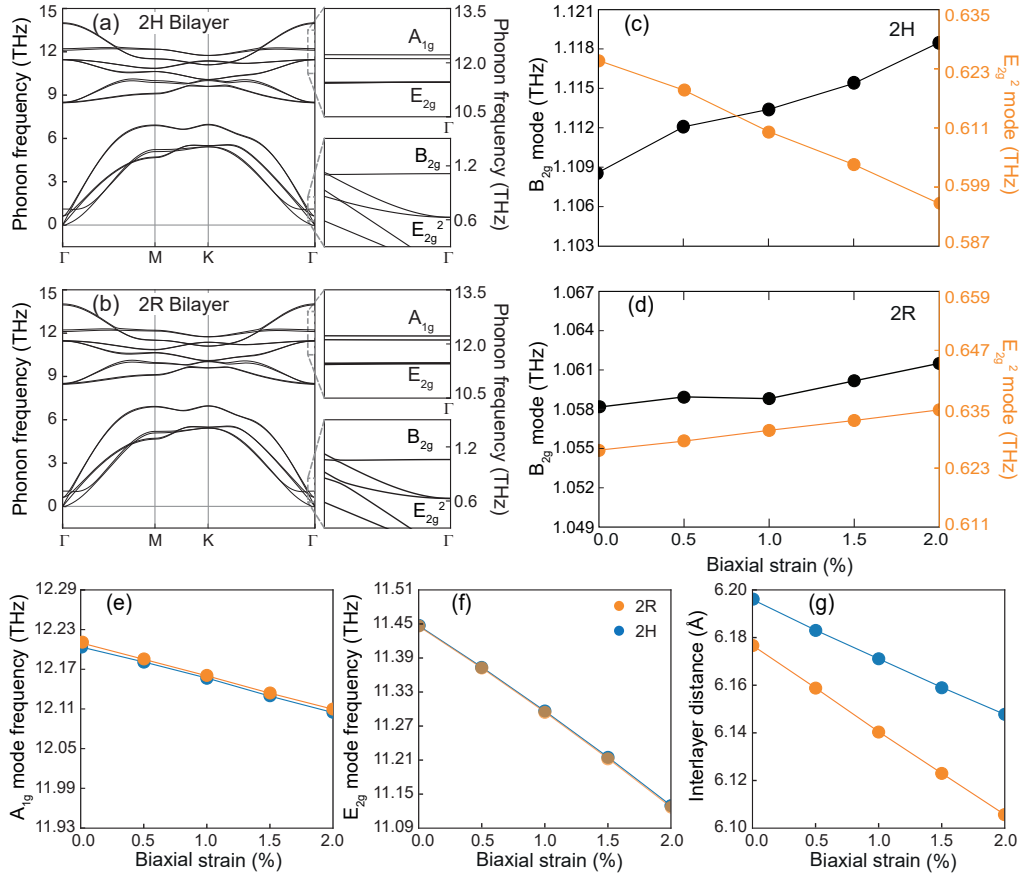


FIG. S2. Vibrational properties of 2H and 2R MoS<sub>2</sub> bilayers using the DFT-D3 approximation. Phonon dispersion of (a) 2R and (b) 2R bilayers with a magnified view at  $\Gamma$  highlighting the  $B_{2g}$  and  $E_{2g}^2$  modes, as well as the intralayer phonon branches. Theoretical interlayer low frequency modes for (c) 2H and (d) 2R. The difference between the minimum and maximum limits on the y-axis is  $0.6 \text{ cm}^{-1}$  for  $B_{2g}$  mode and  $16 \text{ cm}^{-1}$  for  $E_{2g}^2$  mode in both phases.  $A_{1g}$  (e) and  $E_{2g}$  (f) modes obtained for 2H (orange) and 2R (light blue) phase. (g) Interlayer distance between the two monolayers for both phases under biaxial strain.

## S5. SUBSTRATE-DEPENDENT HIGH FREQUENCY RAMAN MODES OF 2H-MOS<sub>2</sub> BILAYERS

Figure S3(a) present a representative Raman spectra showing the out-of-plane  $A_{1g}$  mode of as-grown ( $\text{SiO}_2$  and  $\text{Si}_3\text{N}_4$ ) and transferred MoS<sub>2</sub> bilayers, whose peaks are fitted with Lorentzian profiles. The  $A_{1g}$  mode exhibits only subtle shifts in frequency with substrate variations, indicating that the  $A_{1g}$  phonon mode is not significantly affected by biaxial tensile strain. In panel (b), a representative Raman spectra showing the in-plane (*intralayer*)  $E_{2g}$  mode of as-grown ( $\text{SiO}_2$  and  $\text{Si}_3\text{N}_4$ ) and transferred MoS<sub>2</sub> bilayers, whose peaks are fitted with Lorentzian profiles. The  $E_{2g}$  peaks show a sizable redshift with increasing tensile strain.

## S6. TRANSFER OF PVD-GROWN MOS<sub>2</sub>

The nail polish transfer method [13] was used to transfer PVD-grown MoS<sub>2</sub> bilayer islands on  $\text{SiO}_2/\text{Si}$  to another  $\text{SiO}_2/\text{Si}$  substrate to release strain. First, we placed a small square-cut polydimethylsiloxane (PDMS) on the edge of a glass slide, which we then covered with scotch tape. We put a drop of nail polish on the PDMS and then annealed the slide at  $90^\circ\text{C}$  for 5 minutes. Next, we pressed the nail polish stamp over the flake that needed to be transferred from the growth substrate and heated the substrate to  $80^\circ\text{C}$ . After that, we allowed the system to cool down to room temperature, and then we lifted the nail polish stamp to pick up the flake from the growth substrate. Finally, we pressed the nail polish stamp onto a fresh Si substrate with 90 nm of thermally grown  $\text{SiO}_2$ . The substrate is heated to  $120^\circ\text{C}$ . After the heating, the nail polish stamp is pulled up slowly, leaving MoS<sub>2</sub> bilayer islands along with nail polish on the substrate. Acetone and isopropyl alcohol are used to remove the nail polish. Figure S4 shows the optical

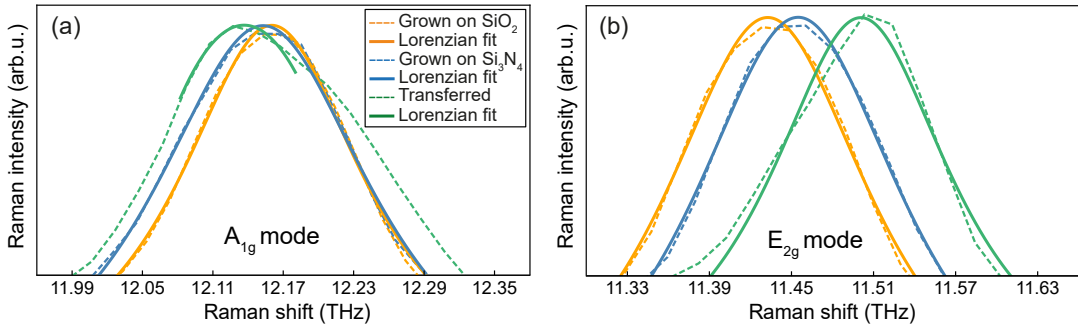


FIG. S3. (a) Raman spectra showing the out-of-plane  $A_{1g}$  mode of as-grown ( $\text{SiO}_2$  and  $\text{Si}_3\text{N}_4$ ) and transferred  $\text{MoS}_2$  bilayers. (b) Representative Raman spectra showing the in-plane (*intralayer*)  $E_{2g}$  mode of as-grown ( $\text{SiO}_2$  and  $\text{Si}_3\text{N}_4$ ) and transferred  $\text{MoS}_2$  bilayers.

micrograph of the transferred  $\text{MoS}_2$  flakes.

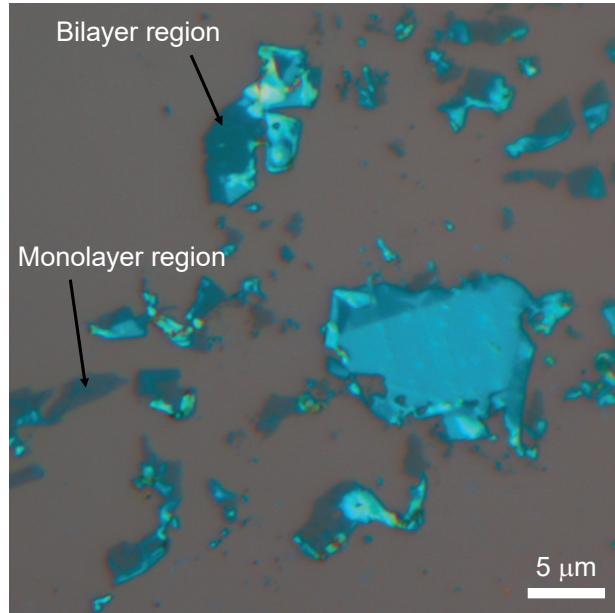


FIG. S4. Optical microscopy image of PVD-grown  $\text{MoS}_2$  flakes transferred onto a  $\text{SiO}_2/\text{Si}$  substrate. The contrast difference distinguishes the monolayer and bilayer regions, as indicated.

## S7. RAMAN SPECTRA OF SHEAR AND BREATHING MODES OF 2H-MOS<sub>2</sub> BILAYERS ON SIO<sub>2</sub> AND SI<sub>3</sub>N<sub>4</sub>.

In Fig. S5 we present representative low-frequency Raman spectra of  $\text{MoS}_2$  grown on  $\text{SiO}_2$  and  $\text{Si}_3\text{N}_4$  substrates, showing the shear ( $E_{2g}^2$ ) and layer-breathing ( $B_{2g}$ ) modes. The Stokes and anti-Stokes peaks are shown with Lorenzian fits. We emphasize showing the shear ( $E_{2g}^2$ ) and layer-breathing ( $B_{2g}$ ) modes

## S8. POLARIZATION-RESOLVED SHG OF 2R-MOS<sub>2</sub>BILAYER

In addition to the SHG intensity maps and spectra shown in the main text, the isotropic intensity for polarization-resolved SHG of the 2R- $\text{MoS}_2$  bilayer is shown in Fig. S6.

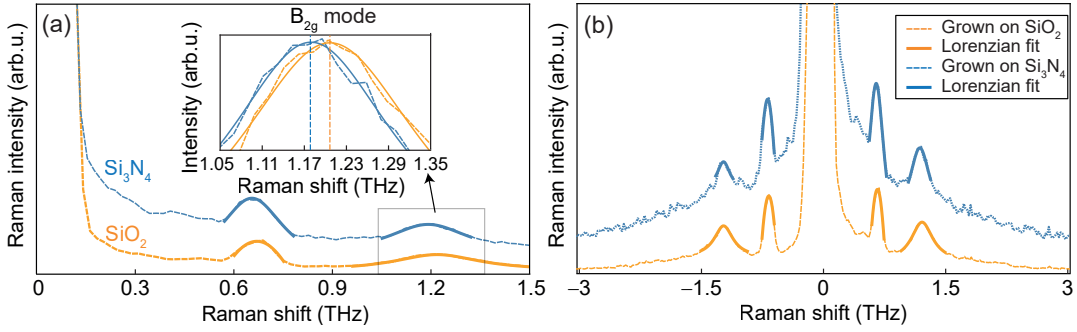


FIG. S5. (a) Low-frequency Raman spectra of MoS<sub>2</sub> grown on SiO<sub>2</sub> and Si<sub>3</sub>N<sub>4</sub> substrates. The inset highlights the B<sub>2g</sub> mode fitted with Lorentzian profiles. (b) A representative Raman spectra showing Stokes and anti-Stokes peaks with Lorentzian fits.

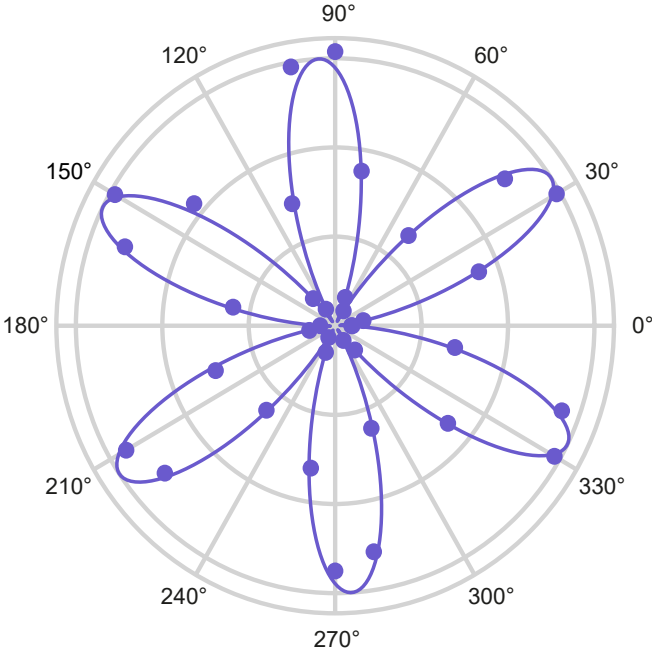


FIG. S6. The symmetric six-lobed pattern reflects that the in-plane crystal symmetry is well preserved (*i.e.*, there are no directionally-preferred distortions of the MoS<sub>2</sub> bilayer), confirming its biaxial strain.

### S9. STRAIN EVOLUTION OF INTERLAYER VIBRATION IN 2R-MOS<sub>2</sub>

Figures S7(a,b) present the strain response of 2R-MoS<sub>2</sub> samples grown on Si<sub>3</sub>N<sub>4</sub> and SiO<sub>2</sub>, while panel Fig. S7(c) provides a comparison with the same modes calculated using DFT. Theory and experiment follow the same trend under biaxial strain. The differences between the two substrates are on the order of 0.030 THz (0.15 THz) for the E<sub>2g</sub><sup>2</sup> (B<sub>2g</sub>) mode, in good agreement with the theoretical results (Fig. S7(c)). The interlayer distance, included in Fig. S7(d), decreases with increasing strain, consistent with the Poisson effect.

### S10. RAMAN SPECTRUM OF A 2H-MOS<sub>2</sub> BILAYER AS-GROWN ON SIO<sub>2</sub> AND WHEN TRANSFERRED.

Figure S8 shows a low-frequency Raman spectrum of a strain-released 2H MoS<sub>2</sub> bilayer on a SiO<sub>2</sub>. A considerable shift is shown in inset of Figure S8(a). Figure S8(b) shows a corresponding zoomed out view including both Stokes and anti-Stokes peaks.

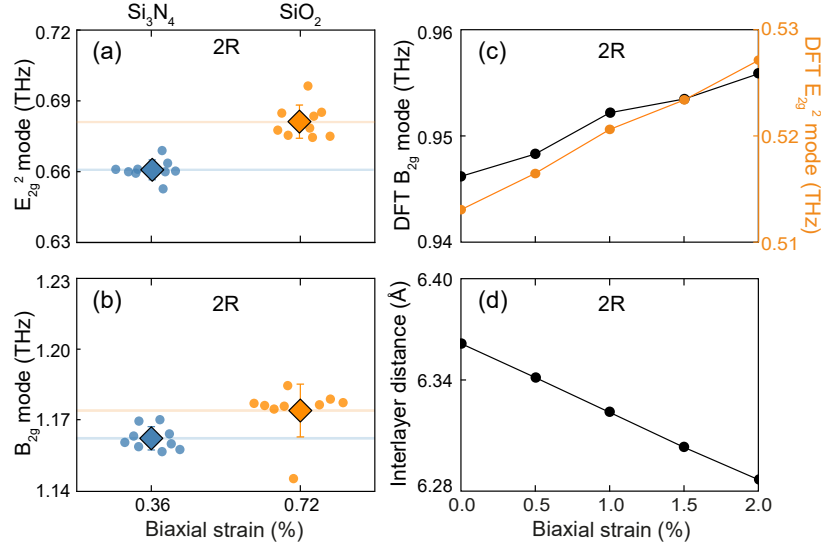


FIG. S7. (a,b) E<sub>2g</sub><sup>2</sup> mode frequencies (a) and B<sub>2g</sub> mode frequencies (b) as a function of biaxial strain controlled by Si<sub>3</sub>N<sub>4</sub> and SiO<sub>2</sub>. (c) Density functional theory (DFT) calculations of the breathing (black) and shear (orange) mode frequencies for 2R-MoS<sub>2</sub> under biaxial tensile strain. (d) DFT calculation of the interlayer distance between the two monolayers for 2R-MoS<sub>2</sub> under biaxial strain.

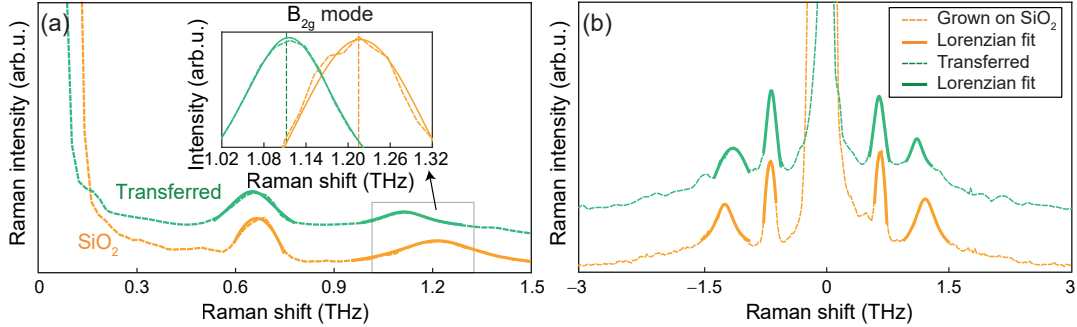


FIG. S8. (a) Representative low-frequency Raman spectra of as-grown and transferred 2H bilayer MoS<sub>2</sub> on SiO<sub>2</sub>, showing the E<sub>2g</sub><sup>2</sup> and B<sub>2g</sub> modes. The inset highlights the B<sub>2g</sub> mode fitted with Lorentzian profiles. (b) A wider-range Raman spectra showing Stokes and anti-Stokes peaks which are fitted with Lorentzian profiles.

## S11. DERIVATION OF EFFECTIVE POISSON'S RATIO

To quantify the vertical coupling strength using a single effective parameter, we assume that the bilayer behaves as a continuum elastic medium [14]. Under in-plane stress ( $\sigma_{zz} = 0$ ) and equi-biaxial loading ( $\sigma_{xx} = \sigma_{yy} = \sigma_{\parallel}$ ), the strains are given by:

$$\varepsilon_{\parallel} = \frac{1}{Y} [\sigma_{\parallel} - \nu_{\text{eff}} (\sigma_{\parallel} + 0)] = \frac{\sigma_{\parallel}}{Y} (1 - \nu_{\text{eff}}), \text{ and} \quad (\text{S2})$$

$$\varepsilon_{\perp} = \frac{1}{Y} [0 - \nu_{\text{eff}} (\sigma_{\parallel} + \sigma_{\parallel})] = -\frac{2\nu_{\text{eff}}\sigma_{\parallel}}{Y}. \quad (\text{S3})$$

Taking the ratio of the vertical strain to the in-plane strain eliminates the Young modulus  $Y$  and stress  $\sigma_{\parallel}$ :

$$\frac{\varepsilon_{\perp}}{\varepsilon_{\parallel}} = \frac{-2\nu_{\text{eff}}}{1 - \nu_{\text{eff}}}. \quad (\text{S4})$$

Solving this expression for  $\nu_{\text{eff}}$  yields the effective Poisson's ratio in terms of the geometric strain contraction:

$$\nu_{\text{eff}} = \frac{-\varepsilon_{\perp}/\varepsilon_{\parallel}}{2 - (\varepsilon_{\perp}/\varepsilon_{\parallel})}. \quad (\text{S5})$$

## S12. ESTIMATING THE VERTICAL STRAIN RATIO

For a hexagonal crystal system (in-plane isotropic with the  $c$ -axis along  $z$ ), the stress in the out-of-plane direction ( $\sigma_{zz}$ ) is related to the strains by the stiffness tensor component:

$$\sigma_{zz} = C_{13}\varepsilon_{xx} + C_{13}\varepsilon_{yy} + C_{33}\varepsilon_{zz}. \quad (\text{S6})$$

In our experiment, the bilayer is subjected to equi-biaxial in-plane tension ( $\varepsilon_{xx} = \varepsilon_{yy} = \varepsilon_{\parallel}$ ) and the vertical direction is free to relax ( $\sigma_{zz} = 0$ ). Substituting these conditions into the equation yields:

$$0 = 2C_{13}\varepsilon_{\parallel} + C_{33}\varepsilon_{\perp}. \quad (\text{S7})$$

Rearranging this terms provides the theoretical ratio between the induced vertical compression ( $\varepsilon_{\perp}$ ) and the applied in-plane strain ( $\varepsilon_{\parallel}$ ):

$$\frac{\varepsilon_{\perp}}{\varepsilon_{\parallel}} = -2 \frac{C_{13}}{C_{33}}. \quad (\text{S8})$$

This relation was used to estimate the effective Poisson ratio from literature in Table I of the main text.

---

\* [hnakamur@uark.edu](mailto:hnakamur@uark.edu)

- [1] S. Patel, T. Faltermeier, S. Puri, R. Rodriguez, K. Reynolds, S. Davari, C. McPherson, H. O. H. Churchill, N. J. Borys, and H. Nakamura, Biaxial strain tuning of excitons in monolayer MoSe<sub>2</sub> by high-temperature physical vapor deposition, *Phys. Rev. B* **110**, 245310 (2024).
- [2] G. Kresse and J. Furthmüller, Efficiency of ab-initio total energy calculations for metals and semiconductors using a plane-wave basis set, *Comput. Mater. Sci.* **6**, 15 (1996).
- [3] J. Klimeš, D. R. Bowler, and A. Michaelides, Chemical accuracy for the van der Waals density functional, *J. Phys. Condens. Matter* **22**, 022201 (2009).
- [4] J. P. Perdew, K. Burke, and M. Ernzerhof, Generalized gradient approximation made simple, *Phys. Rev. Lett.* **77**, 3865 (1996).
- [5] S. Grimme, J. Antony, S. Ehrlich, and H. Krieg, A consistent and accurate ab initio parametrization of density functional dispersion correction (DFT-D) for the 94 elements H-Pu, *J. Chem. Phys.* **132** (2010).
- [6] A. Togo, L. Chaput, T. Tadano, and I. Tanaka, Implementation strategies in phonopy and phono3py, *J. Phys. Condens. Matter* **35**, 353001 (2023).
- [7] A. Togo, First-principles phonon calculations with phonopy and phono3py, *J. Phys. Soc. Jpn.* **92**, 012001 (2023).
- [8] S. Puri, S. Patel, J. L. Cabellos, L. E. Rosas-Hernandez, K. Reynolds, H. O. H. Churchill, S. Barraza-Lopez, B. S. Mendoza, and H. Nakamura, Substrate interference and strain in the second-harmonic generation from MoSe<sub>2</sub> monolayers, *Nano Lett.* **24**, 13061 (2024).
- [9] G. H. Ahn, M. Amani, H. Rasool, D.-H. Lien, J. P. Mastandrea, J. W. Ager III, M. Dubey, D. C. Chrzan, A. M. Minor, and A. Javey, Strain-engineered growth of two-dimensional materials, *Nat. Commun.* **8**, 608 (2017).
- [10] Y. Ding and B. Xiao, Thermal expansion tensors, Grüneisen parameters and phonon velocities of bulk MT<sub>2</sub> (M= W and Mo; T= S and Se) from first principles calculations, *Rsc Advances* **5**, 18391 (2015).
- [11] R. Roy, D. K. Agrawal, and H. A. McKinstry, Very low thermal expansion coefficient materials, *Annual Review of Materials Science* **19**, 59 (1989).
- [12] A. Sinha, H. Levinstein, and T. Smith, Thermal stresses and cracking resistance of dielectric films (SiN, Si<sub>3</sub>N<sub>4</sub>, and SiO<sub>2</sub>) on Si substrates, *Journal of applied physics* **49**, 2423 (1978).
- [13] K. L. Haley, J. A. Cloninger, K. Cerminara, R. M. Sterbentz, T. Taniguchi, K. Watanabe, and J. O. Island, Heated assembly and transfer of van der Waals heterostructures with common nail polish, *Nanomanufacturing* **1**, 49 (2021).
- [14] L. D. Landau and E. M. Lifshitz, *Theory of Elasticity*, 3rd ed. (Pergamon Press, Oxford, 1986).